Materials Science and Engineering B 289 (2023) 116255

Contents lists available at ScienceDirect

Materials Science & Engineering B

journal homepage: www.elsevier.com/locate/mseb

Self-supporting $NiCo_2O_4$ nanoneedle arrays on atomic-layer-deposited CoO nanofilms on nickel foam for efficient and stable hydrogen evolution reaction

Ning Pang [a], Xin Tong [a,c], Yanping Deng [a], Dayuan Xiong [a,b,*], Shaohui Xu [a], Lianwei Wang [a,c,*], Paul K. Chu [c]

[a] Key Laboratory of Polar Materials and Devices (MOE), Department of Electronics, East China Normal University, 500 Dongchuan Road, Shanghai 200241, PR China
[b] Shanghai Key Laboratory of Multidimensional Information Processing, East China Normal University, 500 Dongchuan Road, Shanghai 200241, PR China
[c] Department of Physics, Department of Materials Science and Engineering, and Department of Biomedical Engineering, City University of Hong Kong, Tat Chee Avenue, Kowloon, Hong Kong, China

ARTICLE INFO

Keywords:
Atomic layer deposition
Nanoneedle arrays
Nanofilms
Hydrogen evolution reaction

ABSTRACT

Owing to easy recycling and the pollution-free nature of hydrogen fuel, electrochemical hydrogen production is attracting increasing attention. In this work, 3D $NiCo_2O_4$ nanoneedle arrays are prepared on porous nickel foam (NF) coated with a cobalt oxide nanofilm (CNF) produced by atomic layer deposition (ALD) to form a stable and robust catalyst for the hydrogen evolution reaction (HER). As a result, the optimized $NiCo_2O_4$@C12NF electrode exhibits excellent catalytic activity with a low overpotential of 96 mV versus RHE at a current density of 10 mA cm^{-2}, small Tafel slope of 50.6 mV dec^{-1}, and outstanding stability for over 25 h in 1 M KOH. The excellent characteristics stem from synergistic effects of the unique nanoneedle arrays, abundant active sites, and short channels at the electrode–electrolyte interface. ALD is demonstrated to be a desirable technique to produce highly efficient HER electrocatalysts for commercial water electrolysis.

1. Introduction

In the context of the energy crisis, hydrogen energy plays a huge role in replacing fossil energy to mitigate environmental pollution and achieve sustainable development. It can be generated from water by electrolysis [1–3], but with the hydrogen evolution reaction in water splitting, high-efficiency catalysts are needed in the hydrogen production process [4,5]. Pt-based precious metals are considered the benchmark HER catalysts due to its excellent performance. However, high prices and scarcity of reserves have restricted large-scale application [6,7] and there is an urgent need to develop alternative HER electrocatalysts with higher natural abundance and lower costs. Hence, the non-precious metal HER electrocatalyst has become a hot research topic and has made great progress. Especially transition metal modified catalysts, like the first row of transition metal oxides, hydroxides, sulfides, nitrides, selenides, phosphides, and polymetallic compounds have attracted much attention [8–16]. Catalysts with a variety of shapes including zero-dimensional (0D) nano-atom clusters, one-dimensional (1D) nanotubes, two-dimensional (2D) nano-films, and other three-dimensional (3D) nanocrystals [17–21] have also been proposed. $NiCo_2O_4$ with spinel structure is a promising candidate material due to its abundant valence changes and strong electron coupling ability. The synergistic effect of the unique nanoarray and the short channel at the electrode - electrolyte interface makes $NiCo_2O_4$ get more and more attention.

The HER exists in the contour of the catalyst, so the surface structure and interfacial reactions acted as an important role in the catalytic performance. Fan et al. [22] have prepared MoS_2 and NiS_2 fixed in 3D nitrogen-doped graphene foam (MoS_2-NiS_2/NGF), which showed good catalytic activity with low overpotential (172 mV at a current density of 10 mA cm^{-2}) in HER. Shao et al. have proposed heterostructures consisting of (Ni, Fe)S_2 nano-boxes and MoS_2 nanoarrays with improved activity and durability [23]. Although studies have been proposed to improve the catalytic performance of $NiCo_2O_4$ by regulating the morphology of $NiCo_2O_4$, according to current reports, the manipulation of atomic layer deposition (ALD) to form CoO nanofilms as a buffer layer

* Corresponding authors at: Key Laboratory of Polar Materials and Devices (MOE), Department of Electronics, East China Normal University, 500 Dongchuan Road, Shanghai 200241, PR China.
E-mail addresses: dyxiong@ee.ecnu.edu.cn (D. Xiong), lwwang@ee.ecnu.edu.cn (L. Wang).

https://doi.org/10.1016/j.mseb.2022.116255
Received 22 September 2022; Received in revised form 20 December 2022; Accepted 27 December 2022
Available online 11 January 2023

between the electrocatalyst and the substrate are very few. By optimizing the interface between the electrocatalyst and substrate, the electrocatalytic activity, stability, and toughness can be improved. Therefore, to find stable and efficient nano-thin film materials with $NiCo_2O_4$ as co-catalyst, It is of great significance to improve the catalytic activity [46–49].

In this work, CoO nanofilms are coated on porous nickel foam (NF) by ALD and then self-supporting $NiCo_2O_4$ nanoneedle arrays are fabricated hydrothermally on the surface. The advantage of this structure is that the CoO layer enhances the contact between the $NiCo_2O_4$ nanoneedle arrays and conductive substrate. The CoO buffer layer reduces the contact resistance while preserving the large specific surface area of the 3D nanoneedle structure together with the low energy barrier between the active materials and conductive layer. The $NiCo_2O_4$@C12NF electrode with CoO as the buffer layer shows excellent characteristics in HER. Such as a low Tafel slope of 50.6 mV dec^{-1} at the current density of 10 mA cm^{-2} and overpotential of 96 mV vs RHE in 1 M KOH electrolyte. The strategy to introduce an oxide buffer layer between the electrocatalytic material and the base material can be extended to improve the performance of other types of HER catalysts.

2. Experimental details

2.1. Chemicals and substrate

Cobalt nitrate hexahydrate ($Co(NO_3)_2$ $6H_2O$), nickel(II) nitrate hexahydrate ($Ni(NO_3)_2$ $6H_2O$), urea ($CO(NH_2)_2$) and potassium hydroxide (KOH, ≥99.5 wt%) were purchased from Sinopharm Group Chemical Reagents. All the chemicals used were analytically pure and without further purification. The Solvents were formulated with 18 MΩ deionized water at room temperature and NF was clipped into size of 1 cm × 2 cm.

2.2. Atomic layer deposition of CoO films

The NF substrate was washed ultrasonically with 1.5 M H_2SO_4 solution (20 mL), and deionized (DI) water for 20 min sequentially. Atomic layer deposition is a special kind of chemical vapor deposition, which is a technique of chemical adsorption and reaction of the vapor precursor on the substrate to form a deposition film by alternating pulse into the reactor. There's only one precursor at a time, independent of each other. Each precursor saturates the surface of the substrate to form a single molecular layer. CoO films of different thicknesses (6, 9, 12 and 15 nm) were deposited on the cleaned NF substrate under a self-made ALD system, and the reaction chamber was preheated to 220 °C before deposition. The pulsed gas (N_2) with a flow rate of 20 sccm was used as the carrier gas for depositing the CoO film. The precursors of bis (cyclopentadienyl)cobalt ($(\eta5\text{-}C_5H_5)_2Co$) and the ozone ($O_3$ from an ozone generator) at a flow rate of 100 sccm were introduced as gas-phase precursors. Meanwhile the cobalt source is stored in a vacuum tank with a controlled temperature of 110 °C. The pulse time of $(\eta5\text{-}C_5H_5)_2Co$ and O_3 was adjusted by vacuum solenoid valves to be 10 s and 1.2 s per pulse, respectively. After setting the sample formula parameters that need to be deposited, the cobalt source and ozone channel are opened. Under the control of the electromagnetic valve, the carrier gas carries the alternating deposition of the two precursors. A layer of CoO nanofilm with uniform texture was deposited on Ni foam and and the color gradually changed from silver-white to brown–red with the increase of thickness. The process was repeated at a deposition rate of about 0.3 Å ALD $cycle^{-1}$, layers with thicknesses of 6, 9, 12, and 15 nm were deposited using 200, 300, 400, and 500 cycles (samples denoted as C6NF, C9NF, C12NF, and C15NF).

2.3. Synthesis of $NiCo_2O_4$ nanoneedle arrays

The solution containing 1.5 mM cobalt nitrate and 0.75 mM nickel nitrate were added to 50 mL of DI water and mixed with 7.5 mM urea as the reducing agent and stirred well to form a purple mixture. The solution was then transferred to a Teflon-lined reactor and the hydrothermal temperature was set at 150 °C for 3 h together with the sample after ALD (C6NF, C9NF, C12NF, and C15NF) for in situ catalyst growth. After the reaction, the uniform $NiCo_2O_4$ nanoneedle arrays on CoO/NF were taken out, rinsed with ethanol and DI water, and dried in a vacuum oven at 80 °C degrees for 6 h. The samples were labeled as $NiCo_2O_4$@C6NF, $NiCo_2O_4$@C9NF, $NiCo_2O_4$@C12NF, and $NiCo_2O_4$@C15NF, respectively, according to the thickness of the intermediate CoO layer.

2.4. Materials characterization

The electrode physical characterization was used scanning electron microscopy (SEM) and EDS by the Zeiss Gemini 450 field-emission SEM. Transmission electron microscopy (TEM) was performed on the JEOL JEM-2010. Atomic force microscopy (AFM) was observed by Dimension ICON. X-ray diffraction (XRD) was determined on the Rigaku RINR2000 with Cu K_α radiation ($\lambda = 1.5406$ Å). X-ray photoelectron spectroscopy (XPS) were carried out on AXIS ULTRA DLD XPS with Mg K_α X-ray. The Raman scattering spectra were acquired on the T6400 Jobin Yvon triple monochromator with a 514 nm laser source.

2.5. Electrochemical measurements

A three-electrode system was carried out for electrochemical measurements. Saturated calomel electrode (SCE) was used as the reference electrode, carbon rod was used as the counter electrode, and the composite was prepared as the working electrode on an electrochemical workstation (VMP-3, Biologic SAS) in 1 M KOH at room temperature. The cyclic voltammograms (CV) was collected from −0.45 to 1.85 V vs RHE. The current density was based on the electrode area and CV was carried out to calculate the capacitance (C_{dl}) [24]. The linear sweep voltammetry (LSV) curves were acquired with a scan rate of 5 mV s^{-1} and the potentials were iR- compensated, relative to the ohmic resistance of the solution. Electrochemical impedance spectroscopy (EIS) was conducted with unbiased potential while the frequency ranged from 1 MHz to 100 mHz.

3. Results and discussion

3.1. Materials characterization

The strategy to synthesize $NiCo_2O_4$ nanoneedle arrays on nickel foam coated with CoO nanofilms is schematically shown in Fig. 1. CoO nanolayers with four different thicknesses are prepared on NF pretreated by ALD (denoted as C6NF, C9NF, C12NF, and C15NF). The sample is placed in the Triton X-100 solution for 2 min and the solution and sample react hydrothermally at 150 ℃ for 3 h to produce the $NiCo_2O_4$ nanoneedle arrays uniformly on CoO/NF. The unique nano-arrays increase the active sites and specific surface area. At the same time, the CoO nanolayer deposited by ALD modulates the interface between the nickel foam substrate and $NiCo_2O_4$ to produce desirable effects such as shorter channels at the electrode–electrolyte interface. Fig. 2(a-f) depict the SEM images of $NiCo_2O_4$ with different morphologies. Fig. 2(c, d) shows the urchin-like nano-structure of $NiCo_2O_4$@C12NF, consists of nanoneedles with a length of about 2 μm and diameter of about 100 nm. For comparison, the SEM images of $NiCo_2O_4$@C9NF (Fig. 2a and b) show that the nanoneedle array grows on the substrate. As the thickness of CoO increases, the nanoneedles on CoO increase and a few urchin-like nano-structure of $NiCo_2O_4$@C15NF was observed from Fig. 2(e-f). Ni, Co, and O are detected from $NiCo_2O_4$@C12NF, the uniform distributions across the surface were confirmed by EDS and the corresponding elemental maps (Fig. 2g). To find out the exact thickness of the sample, we use the Atomic force microscopy (AFM) to characterize the growth

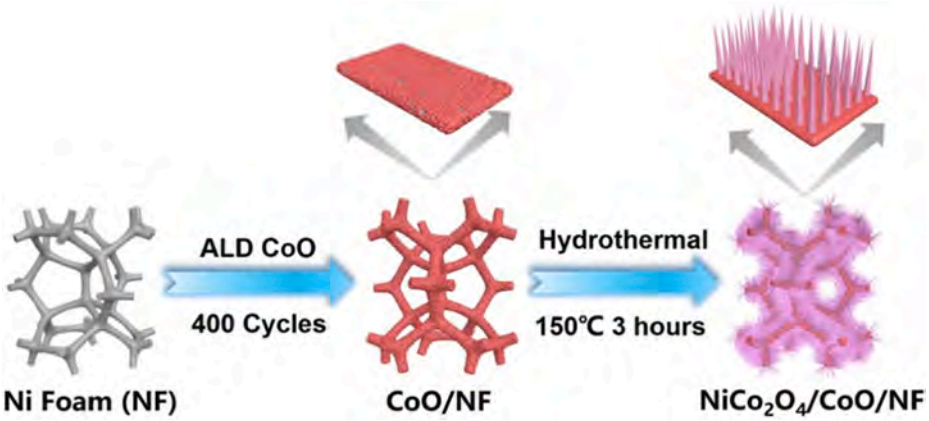

Fig. 1. Demonstration diagram showing the preparation of $NiCo_2O_4$ nanowires on Ni foam deposited with CoO nanofilms.

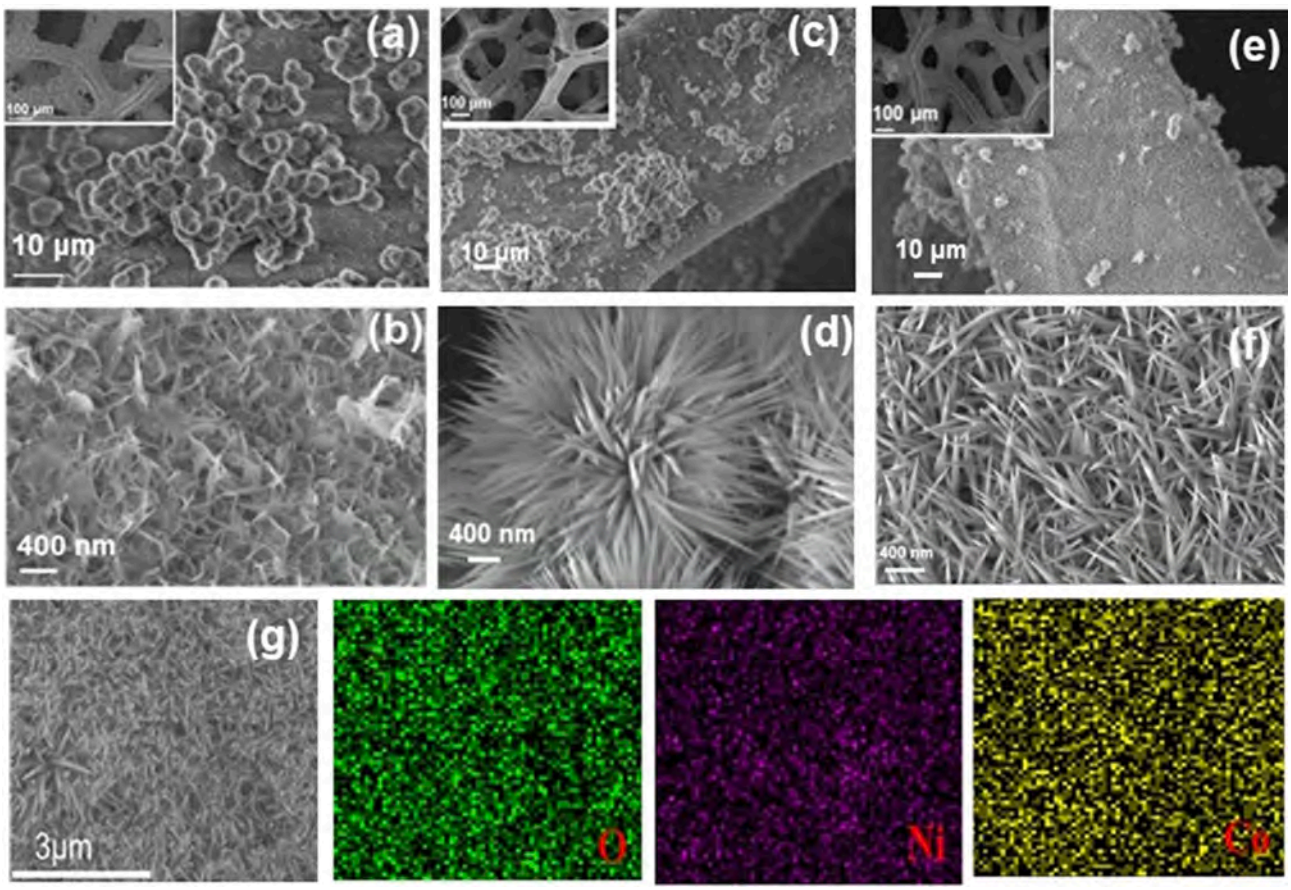

Fig. 2. SEM images of (a) and (b) $NiCo_2O_4$@C12NF;(c) and (d) $NiCo_2O_4$@C12NF; (e) (f) SEM image of $NiCo_2O_4$@C15NF; (g) EDS elemental maps of $NiCo_2O_4$@C12NF.

morphology of CoO nanolayer, and silicon wafers were placed next to the sample preparation to verify the precise growth of CoO. As shown in the Fig. S2, cobalt oxide of different thickness was grown on silicon wafers at the same time. Special membrane tests by AFM showed that CoO of 6, 9, 12, and 15 nm thicknesses accurately grew on the samples.

Fig. 3 was exhibited TEM and HR-TEM images of $NiCo_2O_4$ in different forms. The urchin-like $NiCo_2O_4$ nanostructure consists of a series of closely connected nanoneedles with a diameter of 80 nm and length of 2 μm (Fig. 3(a, b)) in good agreement with SEM (Fig. 2(c,d)). The HR-TEM images in Fig. 3(c, d) reveal lattice spacings of 0.24 nm and 0.28 nm corresponding to the of spinel $NiCo_2O_4$ ((311) and (220) planes, espectively) [25], while the spacing of 0.22 nm is ascribed to the CoO ((200) plane). Fig. 4a shows Raman scattering peaks at 484.0, 526.56, and 691.67 cm^{-1} for the E_g, F_{2g}, and A_{1g} modes of $NiCo_2O_4$ nanoneedles and that at 621.44 cm^{-1} arises from CoO [26]. The peak from the 12 nm CoO film is quite intense suggesting better effects. The surface chemical states of $NiCo_2O_4$@C12/NF have been analyzed by X-ray photoelectron spectroscopy (XPS). Fig. 4(c-f) shows the high-resolution XPS spectra of Ni 2p, Co 2p, C 1 s and O 1 s of the sample, respectively. The Co 2p spectrum discloses the two spin–orbit double peaks of Co $2p_{1/2}$ and Co $2p_{3/2}$ (Fig. 4d). The fitted peaks at 780.4/795.9 eV and 781.8/797.3 eV suggested Co^{3+} and Co^{2+}, respectively

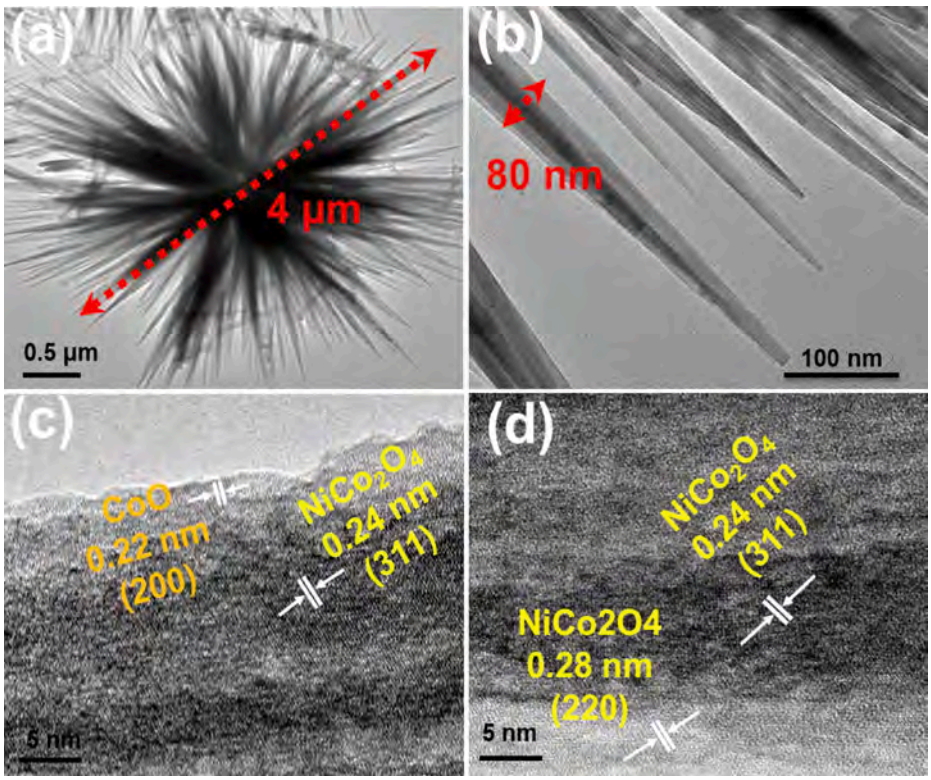

Fig. 3. (a) and (b) TEM images of $NiCo_2O_4$@C12NF; (c) and (d) HR-TEM images of $NiCo_2O_4$@C12NF.

[27] and two satellite peaks were shown at 788.2 eV and 803.7 eV. The Ni 2p spectrum (Fig. 4e) exhibits two spin–orbit double peaks and two satellite peaks marked the existence of Ni^{2+} and Ni^{3+} [28]. And then the O 1 s spectrum shown in Fig. 4f (the peaks at 528.9, 531.4, and 532.8 eV) related to metal–oxygen bond, and adsorbed oxygen, respectively [27]. After CoO is combined with $NiCo_2O_4$, the characteristic peaks of Ni 2p and Co 2p gradually shift to the position of higher binding energy. In general, the increase of binding energy means that the decrease of electron number density leads to the weakening of electron shielding effect. The results show that there is a robust bond between CoO and $NiCo_2O_4$, which promotes the interfacial charge transfer between them. The XRD pattern as shown in Fig. 4b, the representative diffraction peaks of $NiCo_2O_4$ and NF were clearly displayed. And the small diffraction peaks of $NiCo_2O_4$ and CoO in the XRD spectra was caused by the strong diffraction peaks of the nickel substrate and small amounts of active materials. The XRD signature peaks of $NiCo20_4$ were shielded due to the influence of the substrate materials. We conducted XRD tests by collecting the products in the reactor during sample preparation, as shown in Fig. S4. The characteristic peaks of $NiCo_2O_4$ are clearly displayed (PFD# 73–1072), and the xrd data fully prove the successful synthesis of $NiCo_2O_4$.

3.2. Electrocatalytic properties in HER

Fig. 5a compares the CV curves of NF, C6NF, C9NF, C12NF, and C15NF, $NiCo_2O_4$@C9NF, $NiCo_2O_4$@C12NF, and $NiCo_2O_4$@C15NF at a scanning rate of 5 mV s^{-1}. The inset in Fig. 5a appears the A_1 and C_1 peaks of $NiCo_2O_4$@C9NF, $NiCo_2O_4$@C12NF, and $NiCo_2O_4$@C15NF were located at 1.56 V and 1.38 V, whereas the A_1 and C_1 peaks of C9NF, C12NF, and C15NF were at 1.5 V and 1.34 V vs RHE, separately. In addition, the A1 and C1 peaks of NF and C6NF are at 1.45 and 1.29 V vs RHE. Fig. 5b displays the CV curves of $NiCo_2O_4$@C12NF (vs RHE) at scanning rates from 5 to 100 mV s^{-1}. The CV curve exhibits two pairs of distinct redox peaks, indicating that its properties are mainly controlled by the Faraday redox mechanism and a pair of peaks is based on the reversible redox reaction of $Ni^{2+} \leftrightarrow Ni^{3+} + e^-$ [28]. The other weak peak at 1.26 V vs RHE is associated with Co^{2+} / Co^{3+}. The CV curves of $NiCo_2O_4$@C9NF, $NiCo_2O_4$@C15NF, and other samples are shown for comparison in Fig. S4. The electrochemical capacitance of $NiCo_2O_4$@C12NF is owe to the fast and reversible electron transfer process, which involves mainly the Co^{2+} / Co^{3+} and Ni^{2+} / Ni^{3+} redox couples and is most likely to be dominated by OH ions in the alkaline electrolyte [29]. Therefore, the reactions on the surface of the electrodes can be recapitulated as follows [28]:

$$AO + OH^- \leftrightarrow MOOH + e^- \text{ and}$$

$$AOOH + OH^- \leftrightarrow MO_2 + H_2O + e^-,$$

where A represents the Co or Ni cation. To study the process quantitatively, the curves of log V vs log J are plotted in Fig. 5c, where V is the sweeping rate (mV/s) and J is the current density (mA cm^{-2}). The log V vs log J curves exhibit a good linear relationship, suggesting that the redox reaction on NF and C6NF are determined by ion diffusion because the slopes of curves are 0.4 and 0.5 and a value of 0.5 represents a fully diffusion controlled process [30]. However, the redox reaction on C9NF, C12NF, and C15NF, $NiCo_2O_4$@C9NF, $NiCo_2O_4$@C12NF, and $NiCo_2O_4$@C15NF are controlled by mixed diffusion and adsorption, as indicated by the slopes of 0.73, 0.61, 0.69, 0.74, 0.76, and 0.69 because a slope approaching 1 indicates a fully adsorption controlled process [31]. The results show that the electrode under adsorption control has a bigger specific surface area and the reaction rate can be improved. A bigger surface area in contact with the solution increases the electrical double layer capacitance and probability of redox reactions enabling more ions and electrons to participate in the reaction.

To investigate the practicality of $NiCo_2O_4$@C12NF in water electrolysis, the HER characteristics are monitored at a scanning rate of 5 mV s^{-1} in 1.0 M KOH. For contrast, the HER properties of NF, C6NF, C9NF, C12NF, and C15NF, $NiCo_2O_4$@C9NF, and $NiCo_2O_4$@C15NF are also determined based on the same measurement conditions. Fig. 5d exhibits the linear sweeping voltammetry (LSV) polarization curves and

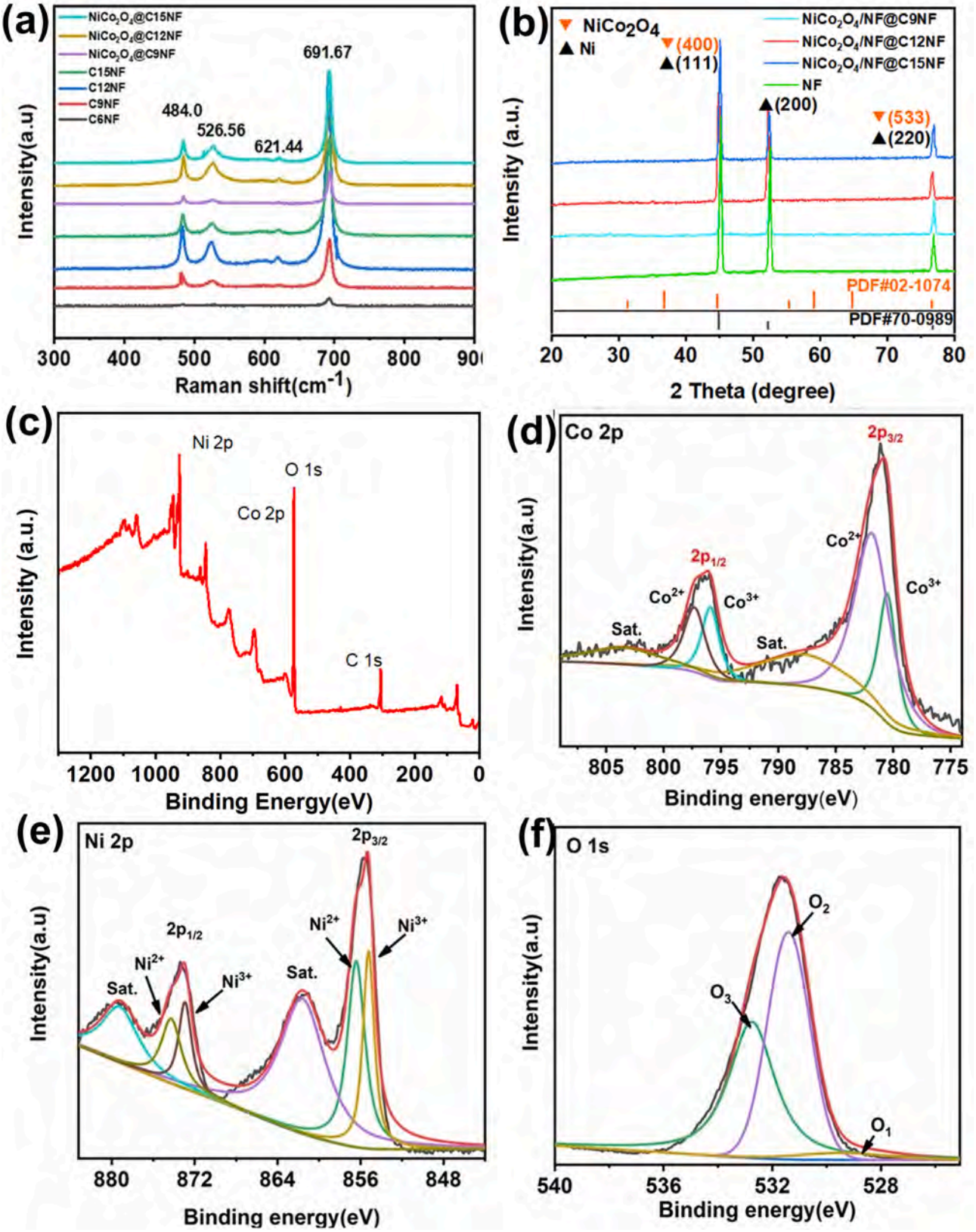

Fig. 4. (a) Raman scattering spectra of the different samples; (b) XRD patterns of the different samples; XPS patterns of (c) $NiCo_2O_4$@C12NF (d) Ni 2p, (e) Co 2p, (f) O 1 s.

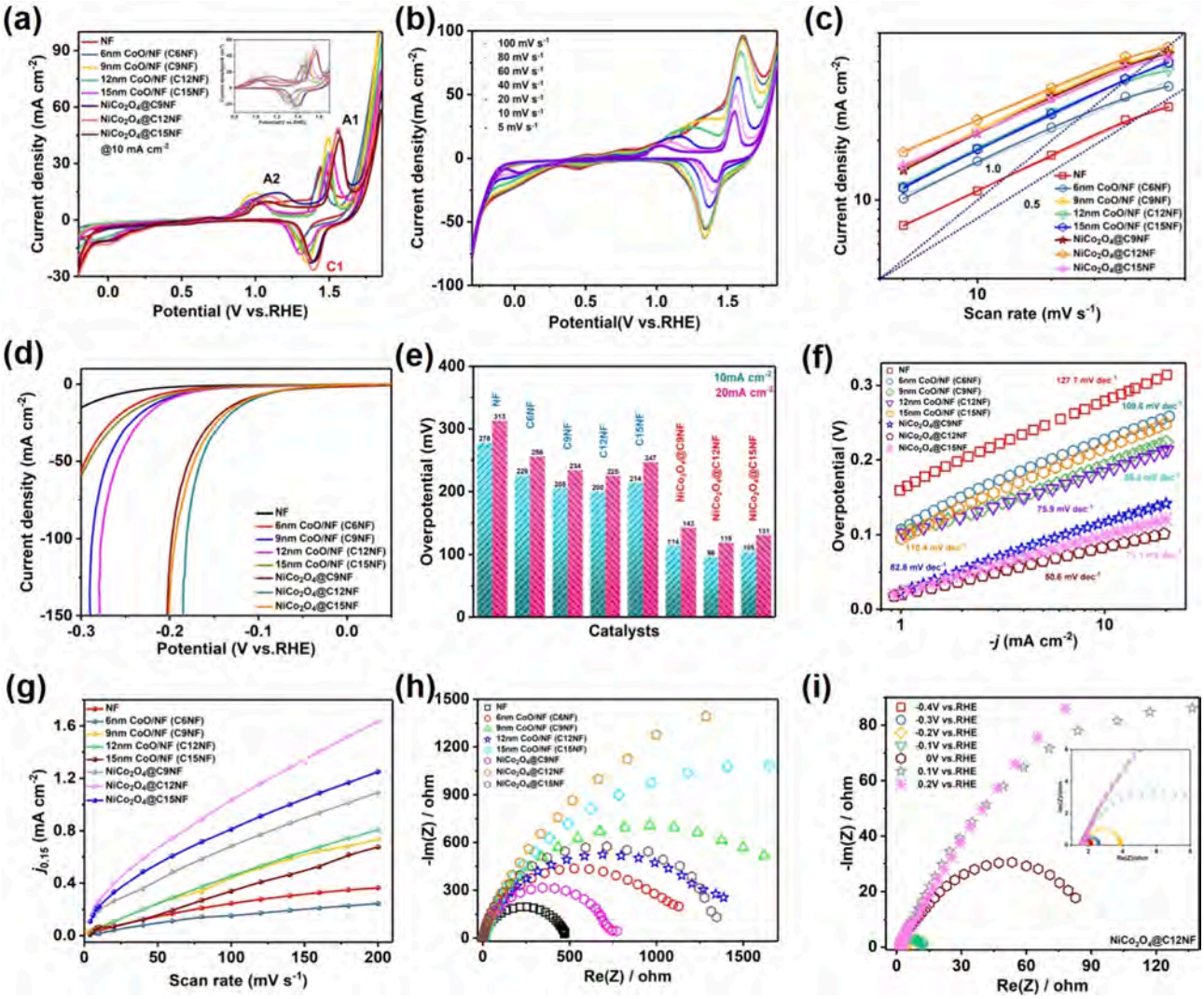

Fig. 5. (a) CV curves of NF, C6NF, C9NF, C12NF, and C15NF, $NiCo_2O_4$@C9NF, $NiCo_2O_4$@C12N,F and $NiCo_2O_4$@C15NF at 10 mV s^{-1}; (b) CV curves of $NiCo_2O_4$@C12NF at different scanning rates; (c) Current densities as a function of scanning rates with different electrodes; (d) HER polarization curves of different electrodes at a scanning rate of 5 mV s^{-1}; (e) Required overpotential to achieve a current density of 10 mA cm^{-2} and 20 mA cm^{-2}; (f) Corresponding Tafel plots for HER; (g) Relationship between the anode current densities and scanning rates in the CV curves; (h) Nyquist plots of the samples; (i) Nyquist plots of $NiCo_2O_4$@C12NF at different potentials in the range from −0.4 to 0.1 V vs RHE.

as shown in Fig. 5e, $NiCo_2O_4$@C12NF shows a noticeably small overpotential of η_{10} = 96 mV at 10 mA cm^{-2}, implying high HER catalytic activity in the alkaline solution. The η_{10} value is fewer than those of NF (278 mV), C6NF (226 mV), C9NF (205 mV), C12NF (200 mV), C15NF (214 mV), $NiCo_2O_4$@C9NF (114 mV), and $NiCo_2O_4$@C15NF (105 mV) under the same conditions. The overpotential shows the same tendency at large current densities of 20 mA cm^{-2}. The Tafel slope of $NiCo_2O_4$@C12NF (50.6 mV dec^{-1}) is also less than those of NF (127.7 mV dec^{-1}), C6NF (109.6 mV dec^{-1}), C9NF (85.4 mV dec^{-1}), C12NF (75.9 mV dec^{-1}), C15NF (110.4 mV dec^{-1}), $NiCo_2O_4$@C9NF (82.8 mV dec^{-1}), and $NiCo_2O_4$@C15NF (71.1 mV dec^{-1}) (Fig. 5f), suggesting a higher HER catalytic rate and the Volmer-Heyrovsky step [33,34]. Therefore, HER proceeds by the following two steps [29–31]:

(1) Volmer: $H_2O(l) + e^- \rightarrow H_{ads} + OH^-(aq)$ and
(2) Heyrovsky: $H_2O(l) + H_{ads} + e^- \rightarrow H_2(g) + OH^-(aq)$,

where H_{ads} denotes one H atom is coupled and adsorbed on the surface on the active site of catalyst. To study the influence of interface engineering on HER, $NiCo_2O_4$/NF with different CoO nanofilms are evaluated. As shown in Fig. 5(d-f), the HER activity increases with the CoO thickness from 0 to 12 nm, but decreases when the CoO nanofilms is increased to 15 nm.

The electrochemical active surface area (ECSA) is positively correlated with the electrochemical double layer capacitance (C_{dl}) [32] and can be used to estimate the electrocatalytic activity. To obtain C_{dl}, CV curves are measured with different scanning rates as illustrated in Fig. S5. Fig. 5g displays a linear correlation between the current density (ΔJ = Ja - Jc) for NF, C6NF, C9NF, C12NF, and C15NF, $NiCo_2O_4$@C9NF, $NiCo_2O_4$@C12NF, and $NiCo_2O_4$@C15NF versus scanning rates at 0.1–0.2 V vs RHE. $NiCo_2O_4$@C12NF has the highest C_{dl} of 28.9 m F·cm^{-2} compared to NF, C6NF, C9NF, C12NF, and C15NF, $NiCo_2O_4$@C9NF, and $NiCo_2O_4$@C15NF. The calculated ECSA values for the other electrodes are 244.92, 51.27, and 7.20 cm^{-2}, respectively. The results reveal improved ECSA and more active site exposure on $NiCo_2O_4$@C12NF.

To elucidate the mechanism, EIS is performed under the opening circuit potential. The charge-transfer resistance (R_{ct}) acquired from the semicircle is interrelated to the phenomenon at the electrode/electrolyte interface region [35]. Fig. 5h shows that $NiCo_2O_4$@C12NF has an R_{ct} of only 65 Ω, which is smaller than those of NF, C6NF, C9NF, C12NF, and C15NF, $NiCo_2O_4$@C9NF, and $NiCo_2O_4$@C15NF. And this result suggests a high-speed electron transfer rate at the catalyst-electrolyte interface.

In order to explore more accurately the impedance changes of the electrodes during the reaction, EIS is performed at potentials from −0.4 to 0.2 V (Fig. 5i and Fig. S6). low frequency region, medium frequency region and high frequency region. The intercept between the curve and the X-axis is called the solution contact resistance, which is generally represented by RS. The semicircle size of the curve depends on the charge transfer efficiency, and the charge transfer resistance is generally represented by Rct. In the end, the linear part of the curve represents the diffusion efficiency, and the CPE capacitor is called a constant phase element. (Fig. S10) the resistance of the system can be divided into three parts, namely the overall internal resistance of the electrode and the electrolyte (R_S), the mass transfer resistance to the electrode due to the concentration difference (Z_f), as well as charge transfer resistance of the double layer at the interface (R_{ct}) [36]. The R_s and the Z_f are remained basically unchanged at different potentials. However, R_{ct} decreases drastically with increasing polarization potentials, which can be used to indicate the activity of catalysts. Hence, the fast transport of electron at the interface between $NiCo_2O_4$@C12NF and electrolyte at high polarization potentials. In order to better explore the electrode performance in the acid solution, three samples of NF, C12/NF and $NiCo_2O_4$@C12/NF

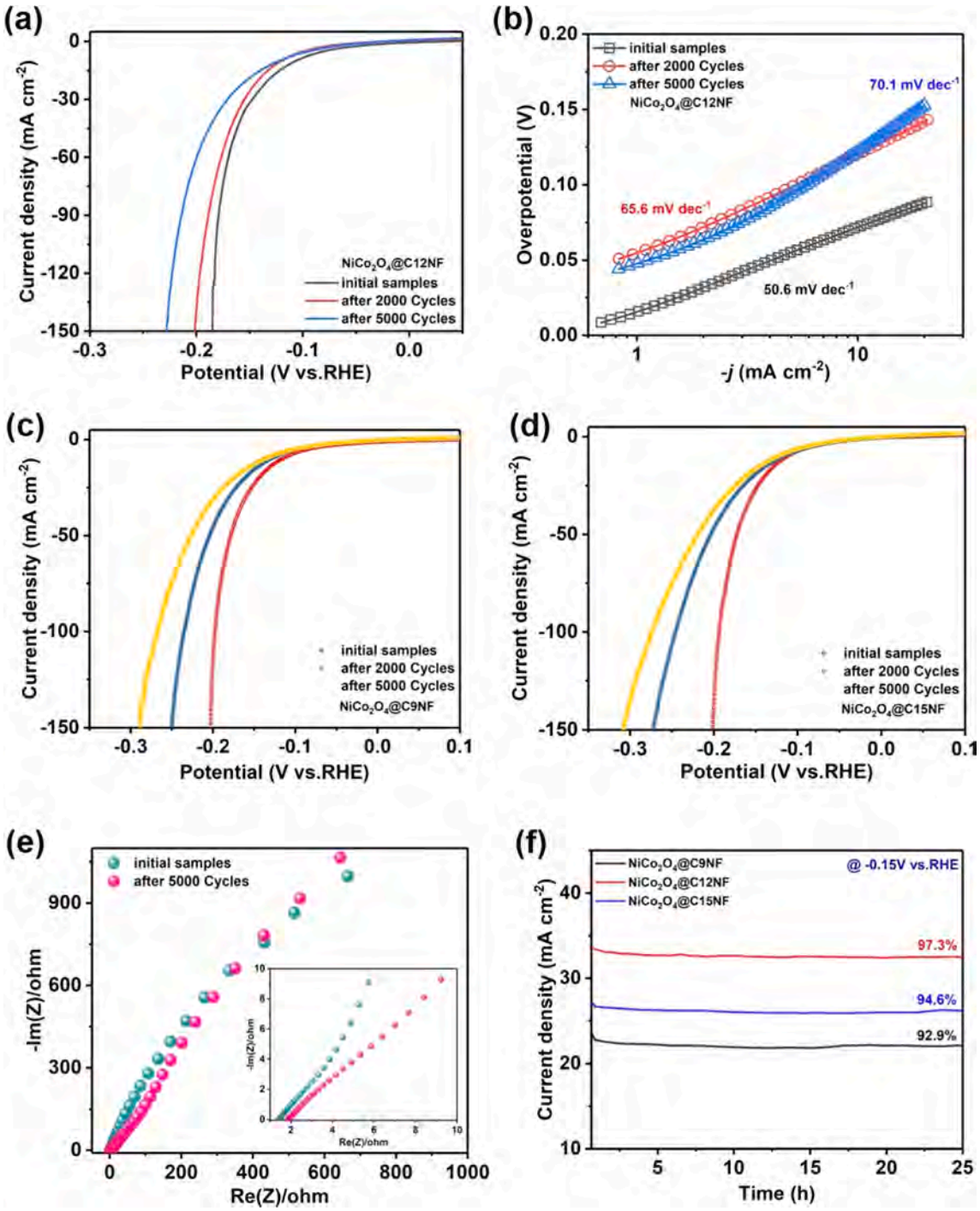

Fig. 6. (a) Polarization curves of $NiCo_2O_4$@C12NF before and after CV; (b) Corresponding Tafel plots; (c) and (d) Polarization curves of $NiCo_2O_4$@C9NF and $NiCo_2O_4$@C15NF before and after CV; (e) Corresponding Nyquist plots; (f) Time-dependent current density curves of $NiCo_2O_4$@C9NF, $NiCo_2O_4$@C12NF, and $NiCo_2O_4$@C15NF in HER at a static potential of −0.15 V versus RHE.

were selected for comparison experiment in 0.5 M H_2So_4. To investigate the effect of acidic solutions on HER, three representative samples (NF, C12NF, and $NiCo_2O_4$@C12NF) were evaluated. As can be seen from Fig. S4, HER activity of the three samples in acidic solution is relatively unsatisfactory, with Tafel slopes of 117.7, 339.6 and 316.1 mV dec^{-1}, respectively, which may be related to the direct reaction of foam nickel substrate in acidic solution. By obtaining Cdl, the electrochemically active surface area of the sample can be assessed. Compared with the alkaline solution test, the Cdl of NF was the highest at 2.3 m F·cm^{-2}. Compared with C12NF (2.04 m F·cm^{-2}) and $NiCo_2O_4$@C12NF (0.9 m F·cm^{-2}), the full reaction with NF may expose relatively more active sites in acidic solutions. To elucidate the mechanism, EIS were performed at open circuit potential. The charge transfer resistance (RCTS) derived from the semicircle is related to the phenomenon at the electrode/electrolyte interface. As can be seen from Fig. 5h, the RCTS of NF are only 45 Ω, smaller than C12NF and $NiCo_2O_4$@C12NF. The results show that the charge transfer resistance increases as the nickel substrate reacts with the solution. To assess stability, long-term cyclic voltammetry was performed for NF, C12NF and $NiCo_2O_4$@C12NF. Fig. 5f shows the stability of the three samples when circulated in solution for more than 10 h. As can be seen from the figure, NF has poor stability in acidic solution and is in a state of constant decay, while CoO/NF maintains good stability for a period of time after declining. Similarly, $NiCo_2O_4$@C12NF has excellent performance under a long-term cycle of more than 25 h. It fully reflects that the heterojunction active materials can maintain excellent stability in both acidic and alkaline environments.

To evaluate the stability, long-term cyclic voltammetry is carried out on $NiCo_2O_4$@C12NF, $NiCo_2O_4$@C9NF, and $NiCo_2O_4$@C15NF. Fig. 6a shows the LSV curves of the initial cycle, after 2,000 CV cycles, and after 5,000 CV cycles of $NiCo_2O_4$@C12NF in 1 M KOH. The corresponding overpotentials are 184, 201, and 227 mV and the overpotentials decrease only slightly for a current density of 150 mA cm^{-2}, which suggesting that $NiCo_2O_4$@C12NF has excellent stability. As illustrated in Fig. 6(c, d), for the same current density, the potentials of $NiCo_2O_4$@C9NF and $NiCo_2O_4$@C15NF decrease to around 86 and 105 mV after 5,000 cycles, respectively. The Tafel slopes of $NiCo_2O_4$@C12NF, $NiCo_2O_4$@C9NF, and $NiCo_2O_4$@C15NF are presented in Fig. 6b and Fig. S7. The decrease observed from $NiCo_2O_4$@C12NF is minimal and the corresponding EIS changes of the three samples are presented in the Fig. 6e and Fig. S8. The Nyquist curves indicate that the impendence of $NiCo_2O_4$@C12NF remains stable after 5,000 cycles but those of $NiCo_2O_4$@C9NF and $NiCo_2O_4$@C15NF are smaller implying catalyst fall-off during the 5,000 cycles test.

The long-term electrochemical stability of $NiCo_2O_4$@C9NF, $NiCo_2O_4$@C12NF, and $NiCo_2O_4$@C15NF at the voltage of −0.15 V is assessed in 1 M KOH displayed in Fig. 6f. There is no obvious decline in the current density further verifying the outstanding stability of $NiCo_2O_4$@C9NF, $NiCo_2O_4$@C12NF, and $NiCo_2O_4$@C15NF. In fact, $NiCo_2O_4$@C12NF shows a slight decrease in current density from 33.8 to 32.5 mA cm^{-2} after 25 h, proving hardly reduced electrochemical activity in HER. In comparison, $NiCo_2O_4$@C9NF shows a current density diminish from 23.8 to 22.1 mA cm^{-2} and that of $NiCo_2O_4$@C15NF decreases from 27.7 to 26.2 mA cm^{-2}. $NiCo_2O_4$@C12NF exhibited the highest polarization current density and maintained a catalytic activity of 97.3 % at a fixed overpotential of 150 mV after 25 h, compared to $NiCo_2O_4$@C9NF (92.9 %), and $NiCo_2O_4$@C15NF (94.6 %). Moreover, the morphology of $NiCo_2O_4$@C12NF is preserved after long-term manipulation. The small overpotential and Tafel slope of $NiCo_2O_4$@C12NF stem from the unique 3D urchin-like nanostructure, abundant electrochemical active sites, large surface area, and special heterojunction with CoO as the buffer layer. Furthermore, the electrochemical characteristics compare well with those of similar catalysts reported in the literature (Fig. 7a) [33–40] and stability is excellent as well (Fig. 7b and Table 1) [41–46,48–56].

4. Conclusion

CoO nanofilms are deposited on NF by atomic layer deposition and then the self-supporting $NiCo_2O_4$ nanoneedles are fabricated hydrothermally on the CoO nanofilms. The composite has a wide surface area, porous nanoarray structure, plentiful active sites, and low reaction barrier. The $NiCo_2O_4$@C12NF nanoneedle array delivers superior HER performance, such as a small overpotential of 96 mV and low Tafel slope of 50.6 mV dec^{-1} at a current density of 10 mA cm^{-2}. Furthermore, the electrode shows outstanding stability in HER for more than 25 h without attenuation in 1 M KOH. The superior HER activity can be attributed to the CoO buffer layer deposited by ALD between the NF substrate and $NiCO_2O_4$ nanoneedle array to reduce the reaction barrier. Our results reveal that ALD is a desirable technique to produce intermediate layers to ameliorate the catalytic characteristics of nanostructured catalysts for HER.

Declaration of Competing Interest

The authors declare that they have no known competing financial interests or personal relationships that could have appeared to influence the work reported in this paper.

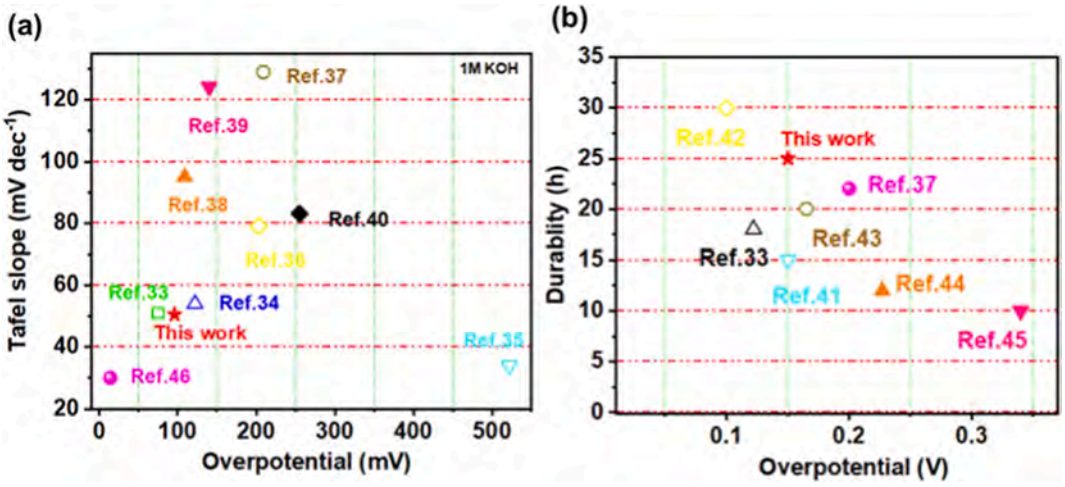

Fig. 7. Comparison with similar catalysts reported in the literature: (a) Overpotentials and Tafel slopes and (b) HER voltages and stability in 1 M KOH.

Table 1
Comparison with similar catalysts reported in the literature: HER *efficiency* in 1 M KOH.

Materials	Electrolytes	Current density [mA cm^{-2}]	Overpotential [mV]	References
$NiCo_2O_4$@CoO/NF	1 M KOH	η_{10}	96	This work
CoNi@NC–$Ru(OH)_xCl_y$	1 M KOH			
Co–Ni–P Film nickel-cobalt-titanium alloy	1 M KOH 1 M KOH	η_{10} η_{10} η_{10}	268 103 125	[48] [49] [50]
$(Co, Ni)_2P/LaF_3$	1 M KOH	η_{10}	94	[51]
Co–Ni–S Nanosheets	1 M KOH	η_{100}	284	[52]
Co–Ni–B	1 M KOH	η_{10}	133	[53]
hyperbranched Co–Ni–P nanocrystals	1 M KOH	η_{10}	119	[54]
$CoNiS_x$/Ni Foam	1 M KOH	η_{10}	123	[55]
CoNi/$CoFe_2O_4$/Ni Foam	1 M KOH	η_{10}	82	[56]

Data availability

Data will be made available on request.

Acknowledgements

This work was jointly supported by the National Natural Science Foundation of China (No. 61991444 and 61774060), Science and Technology Commission of Shanghai Municipality (No. 18DZ2270800), and City University of Hong Kong Strategic Research Grant (SRG) (No. 7005505).

Appendix A. Supplementary material

Supplementary data to this article can be found online at https://doi.org/10.1016/j.mseb.2022.116255.

References

[1] L. Lin, W. Zhou, R. Gao, S. Yao, X. Zhang, W. Xu, S. Zheng, Z. Jiang, Q. Yu, Y.W. Li, C. Shi, X.D. Wen, D. Ma, Low-temperature hydrogen production from water and methanol using Pt/alpha-MoC catalysts, Nature 544 (2017) 80–83.
[2] J. Duan, S. Chen, C. Zhao, Ultrathin metal-organic framework array for efficient electrocatalytic water splitting, Nat. Commun. 8 (2017) 15341.
[3] D. Wu, K. Kusada, S. Yoshioka, T. Yamamoto, T. Toriyama, S. Matsumura, Y. Chen, O. Seo, J. Kim, C. Song, S. Hiroi, O. Sakata, T. Ina, S. Kawaguchi, Y. Kubota, H. Kobayashi, H. Kitagawa, Efficient overall water splitting in acid with anisotropic metal nanosheets, Nat. Commun. 12 (2021) 1145.
[4] G. Chen, T. Wang, J. Zhang, P. Liu, H. Sun, X. Zhuang, M. Chen, X. Feng, Accelerated Hydrogen Evolution Kinetics on NiFe-Layered Double Hydroxide Electrocatalysts by Tailoring Water Dissociation Active Sites, Adv. Mater. 30 (2018) 1706279.
[5] W. Gan, L. Wu, Y. Wang, H. Gao, L. Gao, S. Xiao, J. Liu, Y. Xie, T. Li, J. Li, Carbonized Wood Decorated with Cobalt-Nickel Binary Nanoparticles as a Low-Cost and Efficient Electrode for Water Splitting, Adv. Funct. Mater. (2021) 2010951.
[6] W.J. Jiang, T. Tang, Y. Zhang, J.S. Hu, Synergistic Modulation of Non-Precious-Metal Electrocatalysts for Advanced Water Splitting, Acc. Chem. Res. 53 (2020) 1111–1123.
[7] K. Qi, X. Cui, L. Gu, S. Yu, X. Fan, M. Luo, S. Xu, N. Li, L. Zheng, Q. Zhang, J. Ma, Y. Gong, F. Lv, K. Wang, H. Huang, W. Zhang, S. Guo, W. Zheng, P. Liu, Single-atom cobalt array bound to distorted 1T MoS2 with ensemble effect for hydrogen evolution catalysis, Nat. Commun. 10 (2019) 5231.
[8] Y. Chen, Y. Zheng, X. Yue, S. Huang, Hydrogen evolution reaction in full pH range on nickel doped tungsten carbide nanocubes as efficient and durable non-precious metal electrocatalysts, Int. J. Hydrog. Energy 45 (2020) 8695–8702.
[9] Z. Zhu, H. Yin, C.T. He, M. Al-Mamun, P. Liu, L. Jiang, Y. Zhao, Y. Wang, H. G. Yang, Z. Tang, D. Wang, X.M. Chen, H. Zhao, Ultrathin Transition Metal Dichalcogenide/3d Metal Hydroxide Hybridized Nanosheets to Enhance Hydrogen Evolution Activity, Adv. Mater. 30 (2018) 1801171.
[10] X. Long, H. Lin, D. Zhou, Y. An, S. Yang, Enhancing Full Water-Splitting Performance of Transition Metal Bifunctional Electrocatalysts in Alkaline Solutions by Tailoring CeO_2–Transition Metal Oxides–Ni Nanointerfaces, ACS Energy Lett. 3 (2018) 290–296.
[11] Y. Gao, K. Wang, Z. Lin, H. Song, X. Duan, Z. Peng, S. Yan, Hydrothermal Synthesis of Polyhedral Nickel Sulfide by Dual Sulfur Source for Highly-Efficient Hydrogen Evolution Catalysis, Nanomaterials 10 (2020) 2115.
[12] S. Hussain, M. Hassan, M.S. Javed, A. Shaheen, S.S. Ahmad Shah, M.T. Nazir, T. Najam, A.J. Khan, X. Zhang, G. Liu, Distinctive flower-like $CoNi_2S_4$ nanoneedle arrays (CNS–NAs) for superior supercapacitor electrode performances, Ceram. Int. 46 (2020) 25942–25948.
[13] X. Peng, Y. Yan, X. Jin, C. Huang, W. Jin, B. Gao, P.K. Chu, Recent advance and prospectives of electrocatalysts based on transition metal selenides for efficient water splitting, Nano Energy 78 (2020), 105234.
[14] Y. Gao, H. Li, J. Wang, J. Ma, H. Ren, New Insight on Hydrogen Evolution Reaction Activity of MoP_2 from Theoretical Perspective, Nanomaterials 9 (2019) 1270.
[15] L. Yu, S. Song, B. McElhenny, F. Ding, D. Luo, Y. Yu, S. Chen, Z. Ren, A universal synthesis strategy to make metal nitride electrocatalysts for hydrogen evolution reaction, J. Mater. Chem. A 7 (2019) 19728–19732.
[16] J. Greeley, J.K. Norskov, L.A. Kibler, A.M. El-Aziz, D.M. Kolb, Hydrogen evolution over bimetallic systems: understanding the trends, Chemphyschem 7 (2006) 1032–1035.
[17] J. Zhang, T. Zhu, Y. Wang, J. Cui, J. Sun, J. Yan, Y. Qin, X. Shu, Y. Zhang, J. Wu, C. S. Tiwary, P.M. Ajayan, Y. Wu, Self-assembly of 0D/2D homostructure for enhanced hydrogen evolution, Mater. Today 36 (2020) 83–90.
[18] C. Wang, W. Qi, Y. Zhou, W. Kuang, T. Azhagan, T. Thomas, C. Jiang, S. Liu, M. Yang, Ni-Mo ternary nitrides based one-dimensional hierarchical structures for efficient hydrogen evolution, Chem. Eng. J. 381 (2020).
[19] J. Li, B. Zhang, Q. Song, X. Xu, W. Hou, Sulfur and molybdenum Co-doped graphitic carbon nitride as a superior water dissociation electrocatalyst for alkaline hydrogen evolution reaction, Ceram. Int. 46 (2020) 14178–14187.
[20] M. Lunardon, J. Ran, D. Mosconi, C. Marega, Z. Wang, H. Xia, S. Agnoli, G. Granozzi, Hybrid Transition Metal Dichalcogenide/Graphene Microspheres for Hydrogen Evolution Reaction, Nanomaterials 10 (2020) 2376.
[21] X. Tong, S. Chen, C. Guo, X. Xia, X.Y. Guo, Mesoporous $NiCo_2O_4$ Nanoplates on Three-Dimensional Graphene Foam as an Efficient Electrocatalyst for the Oxygen Reduction Reaction, ACS Appl. Mater. Interfaces 8 (2016) 28274–28282.
[22] P. Kuang, M. He, H. Zou, J. Yu, K. Fan, 0D/3D MoS_2-NiS_2/N-doped graphene foam composite for efficient overall water splitting, Appl. Catal. B 254 (2019) 15–25.
[23] Y. Liu, S. Jiang, S. Li, L. Zhou, Z. Li, J. Li, M. Shao, Interface engineering of (Ni, Fe) S_2@MoS_2 heterostructures for synergetic electrochemical water splitting, Appl. Catal. B 247 (2019) 107–114.
[24] T. Sun, S. Zhao, W. Chen, D. Zhai, J. Dong, Y. Wang, S. Zhang, A. Han, L. Gu, R. Yu, X. Wen, H. Ren, L. Xu, C. Chen, Q. Peng, D. Wang, Y. Li, Single-atomic cobalt sites embedded in hierarchically ordered porous nitrogen-doped carbon as a superior bifunctional electrocatalyst, Proc. Natl. Acad. Sci. U.S.A. 115 (2018) 12692–12697.
[25] X. Gao, H. Zhang, Q. Li, X. Yu, Z. Hong, X. Zhang, C. Liang, Z. Lin, Hierarchical $NiCo_2O_4$ Hollow Microcuboids as Bifunctional Electrocatalysts for Overall Water-Splitting, Angew. Chem. Int. Ed. 55 (2016) 6290–6294.
[26] Y. Liu, Y. Du, W.-K. Gao, B. Dong, Y. Han, L. Wang, Surface phosphorsulfurization of $NiCo_2O_4$ nanoneedles supported on carbon cloth with enhanced electrocatalytic activity for hydrogen evolution, Electrochim. Acta 290 (2018) 339–346.
[27] L. Fang, Z. Jiang, H. Xu, L. Liu, Y. guan, X. Gu, Y. Wang, Crystal-plane engineering of $NiCo_2O_4$ electrocatalysts towards efficient overall water splitting, J. Catal., 357 (2018) 238-246.
[28] V. Artero, M. Chavarot-Kerlidou, M. Fontecave, Wasserspaltung mit Cobalt, Angew. Chem. Int. Ed. 123 (2011) 7376–7405.
[29] H. Fei, J. Dong, M.J. Arellano-Jimenez, G. Ye, N. Dong Kim, E.L. Samuel, Z. Peng, Z. Zhu, F. Qin, J. Bao, M.J. Yacaman, P.M. Ajayan, D. Chen, J.M. Tour, Atomic cobalt on nitrogen-doped graphene for hydrogen generation, Nat. Commun. 6 (2015) 8668.

[30] J. Mao, C.T. He, J. Pei, W. Chen, D. He, Y. He, Z. Zhuang, C. Chen, Q. Peng, D. Wang, Y. Li, Accelerating water dissociation kinetics by isolating cobalt atoms into ruthenium lattice, Nat. Commun. 9 (2018) 4958.
[31] Y. Lei, Y. Wang, Y. Liu, C. Song, Q. Li, D. Wang, Y. Li, Designing Atomic Active Centers for Hydrogen Evolution Electrocatalysts, Angew. Chem. Int. Ed. 59 (2020) 20794–20812.
[32] C. Huang, X. Miao, C. Pi, B. Gao, X. Zhang, P. Qin, K. Huo, X. Peng, P.K. Chu, Mo_2C/VC heterojunction embedded in graphitic carbon network: An advanced electrocatalyst for hydrogen evolution, Nano Energy 60 (2019) 520–526.
[33] P. Jiang, Q. Liu, X. Sun, NiP(2) nanosheet arrays supported on carbon cloth: an efficient 3D hydrogen evolution cathode in both acidic and alkaline solutions, Nanoscale 6 (2014) 13440–13445.
[34] Q. Liu, J. Tian, W. Cui, P. Jiang, N. Cheng, A.M. Asiri, X. Sun, Carbon nanotubes decorated with CoP nanocrystals: a highly active non-noble-metal nanohybrid electrocatalyst for hydrogen evolution, Angew. Chem. Int. Ed. 53 (2014) 6710–6714.
[35] J. Yin, P. Zhou, L. An, L. Huang, C. Shao, J. Wang, H. Liu, P. Xi, Self-supported nanoporous $NiCo_2O_4$ nanowires with cobalt-nickel layered oxide nanosheets for overall water splitting, Nanoscale 8 (2016) 1390–1400.
[36] R. Xu, R. Wu, Y. Shi, J. Zhang, B. Zhang, Ni_3Se_2 nanoforest/Ni foam as a hydrophilic, metallic, and self-supported bifunctional electrocatalyst for both H_2 and O_2 generations, Nano Energy 24 (2016) 103–110.
[37] J. Tian, Q. Liu, A.M. Asiri, X. Sun, Self-supported nanoporous cobalt phosphide nanowire arrays: an efficient 3D hydrogen-evolving cathode over the wide range of pH 0–14, J. Am. Chem. Soc. 136 (2014) 7587–7590.
[38] Y. Zhang, B. Ouyang, J. Xu, S. Chen, R.S. Rawat, H.J. Fan, 3D Porous Hierarchical Nickel-Molybdenum Nitrides Synthesized by RF Plasma as Highly Active and Stable Hydrogen-Evolution-Reaction Electrocatalysts, Adv. Energy Mater. 6 (2016) 1600221.
[39] L. Ma, Y. Hu, R. Chen, G. Zhu, T. Chen, H. Lv, Y. Wang, J. Liang, H. Liu, C. Yan, H. Zhu, Z. Tie, Z. Jin, J. Liu, Self-assembled ultrathin $NiCo_2S_4$ nanoflakes grown on Ni foam as high-performance flexible electrodes for hydrogen evolution reaction in alkaline solution, Nano Energy 24 (2016) 139–147.
[40] C.G. Read, J.F. Callejas, C.F. Holder, R.E. Schaak, General Strategy for the Synthesis of Transition Metal Phosphide Films for Electrocatalytic Hydrogen and Oxygen Evolution, ACS Appl. Mater. Interfaces 8 (2016) 12798–12803.
[41] B. Liu, Y.F. Zhao, H.Q. Peng, Z.Y. Zhang, C.K. Sit, M.F. Yuen, T.R. Zhang, C.S. Lee, W.J. Zhang, Nickel-Cobalt Diselenide 3D Mesoporous Nanosheet Networks Supported on Ni Foam: An All-pH Highly Efficient Integrated Electrocatalyst for Hydrogen Evolution, Adv. Mater. 29 (2017) 1606521.
[42] R. Zhang, X. Wang, S. Yu, T. Wen, X. Zhu, F. Yang, X. Sun, X. Wang, W. Hu, Ternary $NiCo_2P_x$ Nanowires as pH-Universal Electrocatalysts for Highly Efficient Hydrogen Evolution Reaction, Adv. Mater. 29 (2017) 1605502.
[43] H. Sun, X. Xu, Z. Yan, X. Chen, L. Jiao, F. Cheng, J. Chen, Superhydrophilic amorphous Co–B–P nanosheet electrocatalysts with Pt-like activity and durability for the hydrogen evolution reaction, J. Mater. Chem. A 6 (2018) 22062–22069.
[44] D. Liu, Q. Lu, Y. Luo, X. Sun, A.M. Asiri, $NiCo_2S_4$ nanowires array as an efficient bifunctional electrocatalyst for full water splitting with superior activity, Nanoscale 7 (2015) 15122–15126.
[45] R. Chen, H.-Y. Wang, J. Miao, H. Yang, B. Liu, A flexible high-performance oxygen evolution electrode with three-dimensional $NiCo_2O_4$ core-shell nanowires, Nano Energy 11 (2015) 333–340.
[46] S. Ye, F. Luo, Q. Zhang, P. Zhang, T. Xu, Q. Wang, D. He, L. Guo, Y. Zhang, C. He, X. Ouyang, M. Gu, J. Liu, X. Sun, Highly stable single Pt atomic sites anchored on aniline-stacked graphene for hydrogen evolution reaction, Energy Environ. Sci. 12 (2019) 1000–1007.
[47] L. Zhang, R. Si, H. Liu, N. Chen, Q. Wang, K. Adair, Z. Wang, J. Chen, Z. Song, J. Li, M.N. Banis, R. Li, T.K. Sham, M. Gu, L.M. Liu, G.A. Botton, X. Sun, Atomic layer deposited Pt-Ru dual-metal dimers and identifying their active sites for hydrogen evolution reaction, Nat Commun 10 (2019) 4936.
[48] I.J. Hsu, Y.C. Kimmel, X. Jiang, B.G. Willis, J.G. Chen, Atomic layer deposition synthesis of platinum-tungsten carbide core-shell catalysts for the hydrogen evolution reaction, Chem Commun (Camb) 48 (2012) 1063–1065.
[49] W. Wang, S. Xi, Y. Shao, W. Sun, S. Wang, J. Gao, C. Mao, X. Guo, G. Li, Oxide Passivated CoNi@NC-Supported Ru(OH)xCly Cluster as Highly Efficient Catalysts for the Oxygen and Hydrogen Evolution, ACS Sustain. Chem. Eng. 7 (2019) 17227–17236.
[50] Y. Pei, Y. Yang, F. Zhang, P. Dong, R. Baines, Y. Ge, H. Chu, P.M. Ajayan, J. Shen, M. Ye, Oxide Passivated CoNi@NC-Supported Ru(OH)xCly Cluster as Highly Efficient Catalysts for the Oxygen and Hydrogen Evolution, ACS Appl. Mater. Interfaces 9 (2017) 31887–31896.
[51] P. Ganesan, A. Sivanantham, S. Shanmugam, Nanostructured Nickel-Cobalt-Titanium Alloy Grown on Titanium Substrate as Efficient Electrocatalyst for Alkaline Water Electrolysis, ACS Appl. Mater. Interfaces 9 (2017) 12416–12426.
[52] K. Tao, H. Dan, Y. Hai, L. Liu, Y. Gong, LaF(3) Nanosheet-induced Epitaxial Growth: Hollow (Co, Ni)(2)P/LaF(3) Nanotube Arrays Built by Porous Heterojunction Walls Grown on Ni Foam as Active Electrocatalyst for Hydrogen Evolution Reaction, Inorg. Chem. 59 (2020) 7000–7011.
[53] S. Gupta, N. Patel, R. Fernandes, R. Kadrekar, A. Dashora, A.K. Yadav, D. Bhattacharyya, S.N. Jha, A. Miotello, D.C. Kothari, Co-Ni-B nanocatalyst for efficient hydrogen evolution reaction in wide pH range, Appl. Catal. B: Environ. 192 (2016) 126–133.
[54] W. Pei, X. Wang, C. Liu, D. Zhao, C. Wu, K. Wang, Q. Wang, Electrochim. Acta 381 (2021).
[55] W. Lu, X. Li, F. Wei, K. Cheng, W. Li, Y. Zhou, W. Zheng, L. Pan, G. Zhang, Synthesis of hyperbranched Co-Ni-P nanocrystals and their splitting degree dependent HER performances, ACS Sustain. Chem. Eng. 7 (2019) 12501–12509.
[56] S. Li, S. Sirisomboonchai, A. Yoshida, X. An, X. Hao, A. Abudula, G. Guan, Bifunctional CoNi/CoFe2O4 /Ni foam electrodes for efficient overall water splitting at a high current density, J. Mater. Chem. A 6 (2018) 19221–19230.

Supplementary Material

Ning Pang[a], Xin Tong[a, c], Yanping Deng[a], Dayuan Xiong[a, b]*, Shaohui Xu[a], Lianwei Wang[a, c]*, Paul K. Chu[c]

[a] *Key Laboratory of Polar Materials and Devices (MOE), Department of Electronics, East China Normal University, 500 Dongchuan Road, Shanghai 200241, P. R. China*

[b] *Shanghai Key Laboratory of Multidimensional Information Processing, East China Normal University, 500 Dongchuan Road, Shanghai 200241, P. R. China*

[c] *Department of Physics, Department of Materials Science and Engineering, and Department of Biomedical Engineering, City University of Hong Kong, Tat Chee Avenue, Kowloon, Hong Kong, China*

Corresponding Authors:

* L.W. Wang: Tel: +86-021-54345160, Fax: +86-021-54345119, Email: lwwang@ee.ecnu.edu.cn; D. Y. Xiong (Email: dyxiong@ee.ecnu.edu.cn)

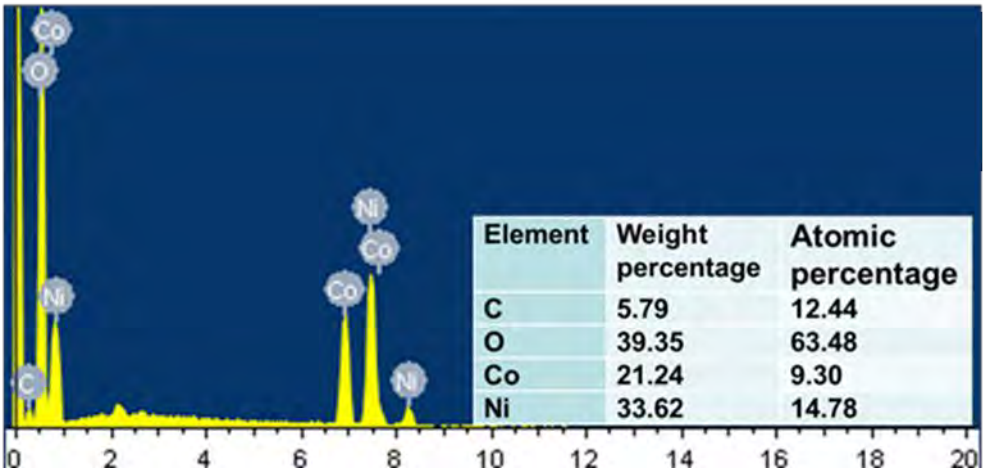

Element	Weight percentage	Atomic percentage
C	5.79	12.44
O	39.35	63.48
Co	21.24	9.30
Ni	33.62	14.78

Fig. S1. EDS spectrum of $NiCo_2O_4$@C12NF.

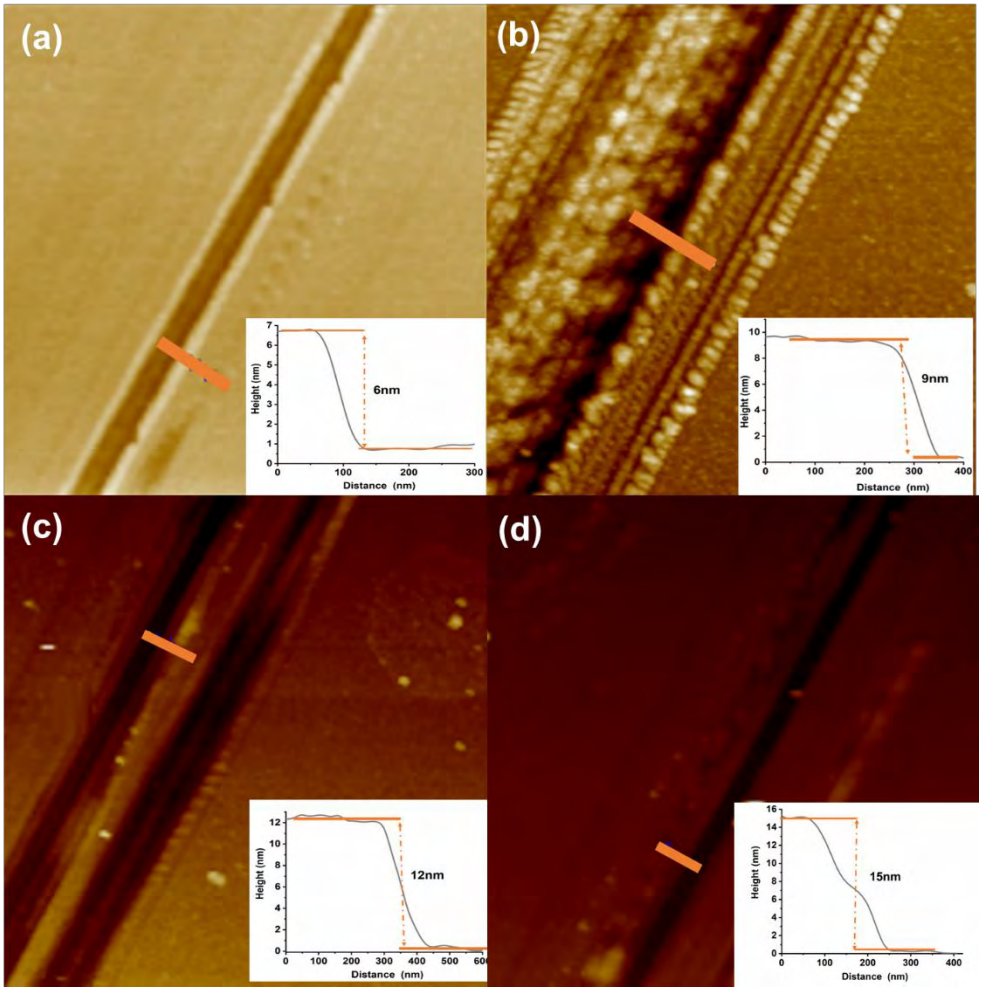

Fig. S2. (a-d) AFM images of 6, 9, 12 and15 nm CoO Nanometer layer.

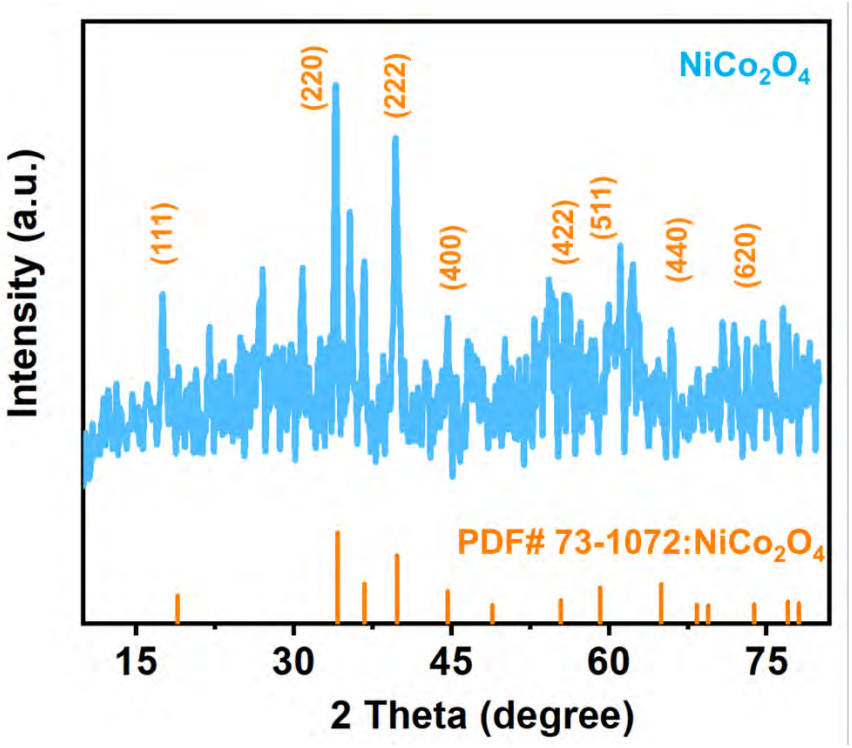

Fig. S3.XRD patterns of the $NiCo_2O_4$ samples

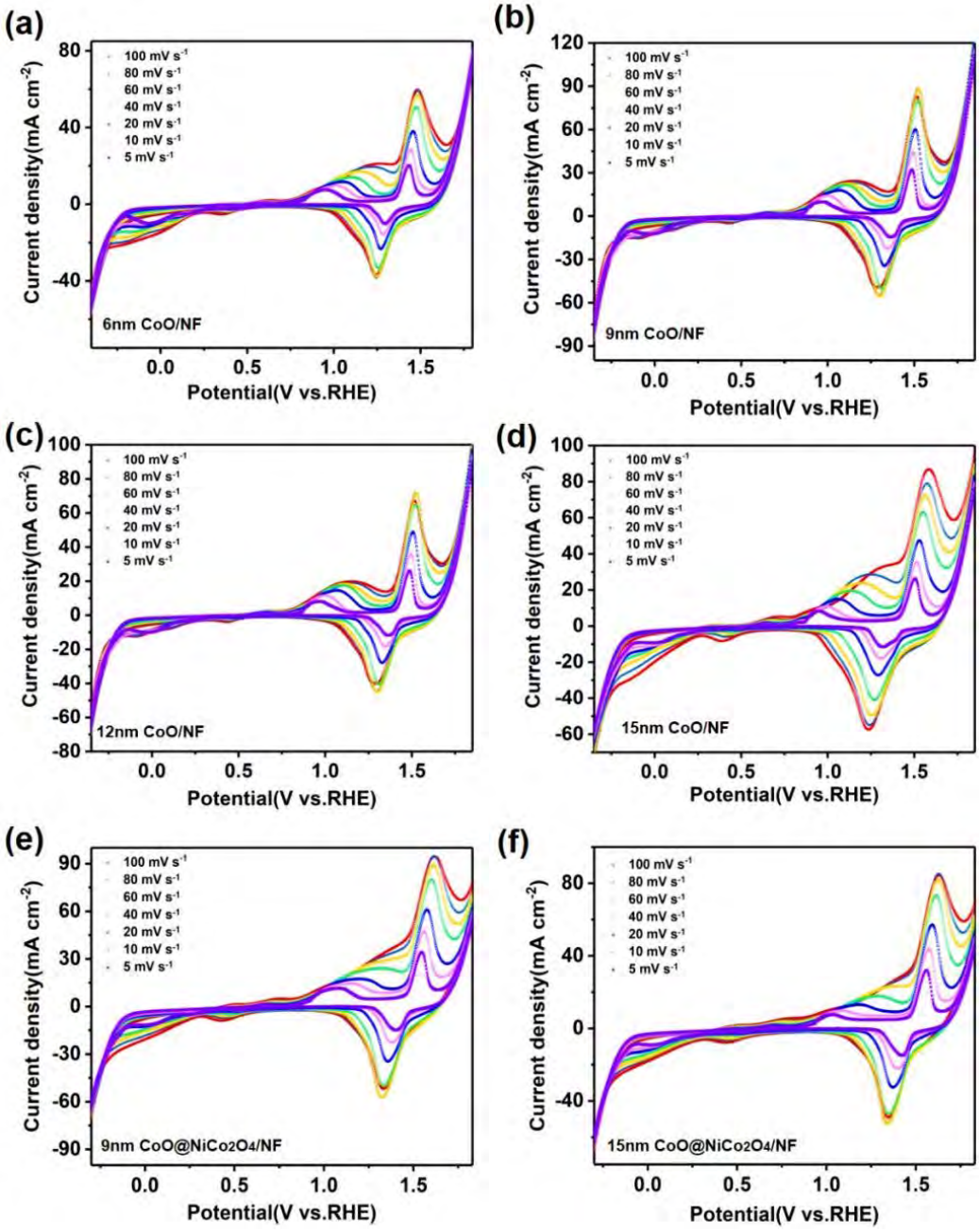

Fig. S4. CV curves of different samples.

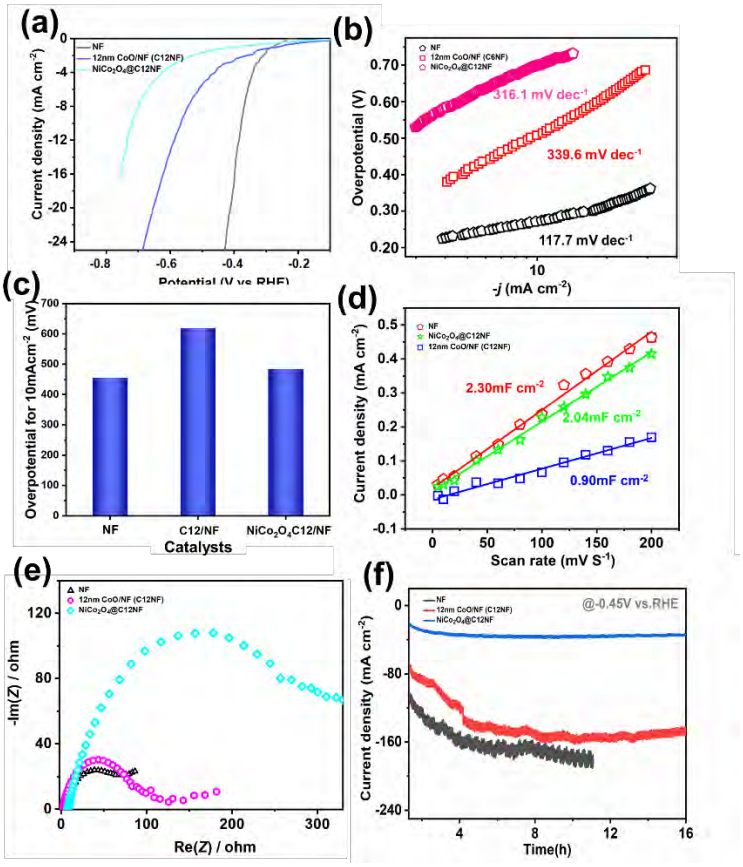

Fig. S5. (a) HER polarization curves of different electrodes at a scanning rate of 5 mV s^{-1}; (b) Corresponding Tafel plots for HER; (c) Required overpotential to achieve a current density of 10 mA cm^{-2}; (d) Relationship between the anode current densities and scanning rates in the CV curves; (e) Nyquist plots of the samples; (f) Time-dependent current density curves of NF, C12NF, and $NiCo_2O_4$@C12NF in HER at a static potential of -0.45 V versus RHE.

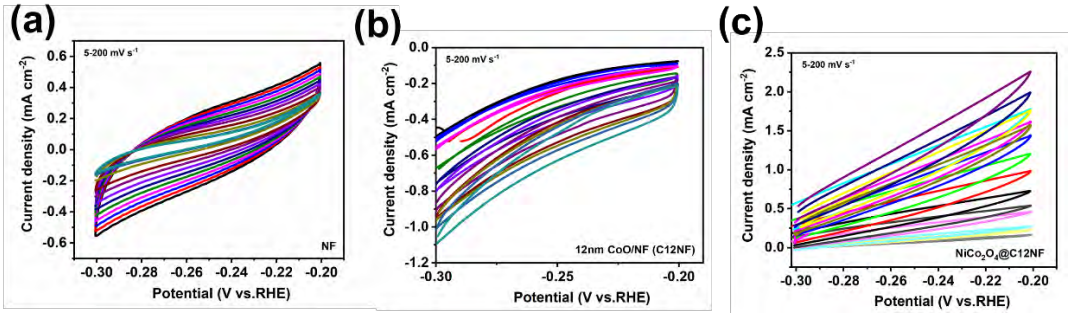

Fig. S6. CV curves of different samples in the range of -0.3~0.2 V vs. RHE and in 0.5M H_2SO_4. Solution.

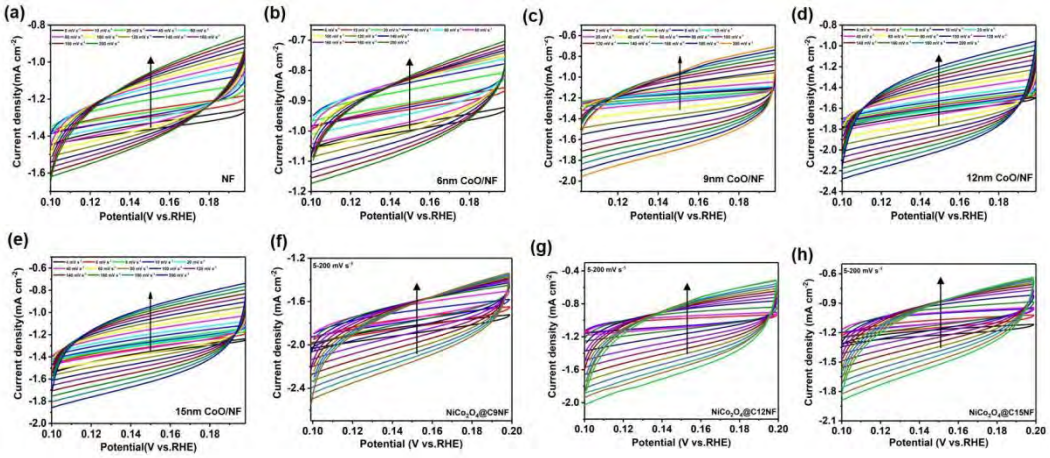

Fig. S7. CV curves of different samples in the range of 0.1~0.2 V vs. RHE.

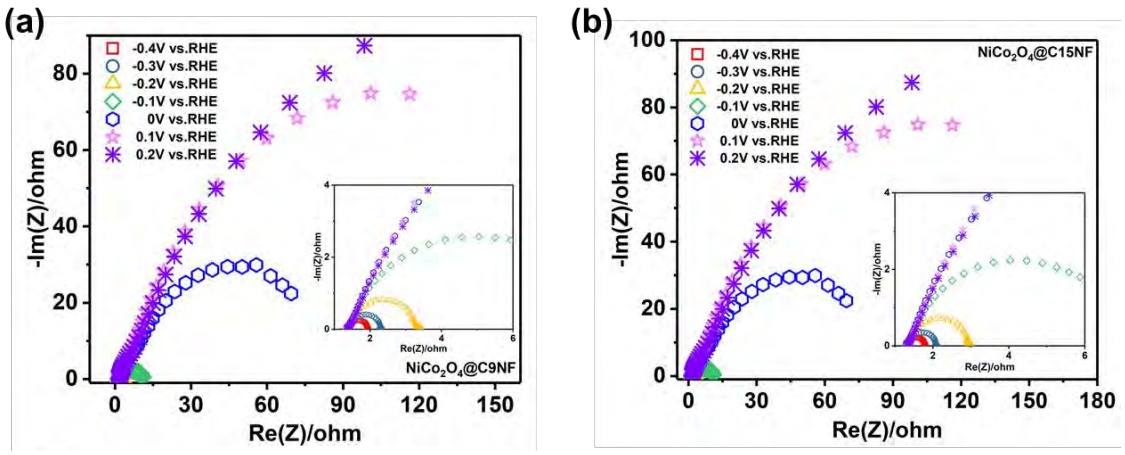

Fig. S8. Nyquist plots of $NiCo_2O_4$@C9NF and $NiCo_2O_4$@C15NF in the potential range between -0.4 and 0.2 V vs. RHE.

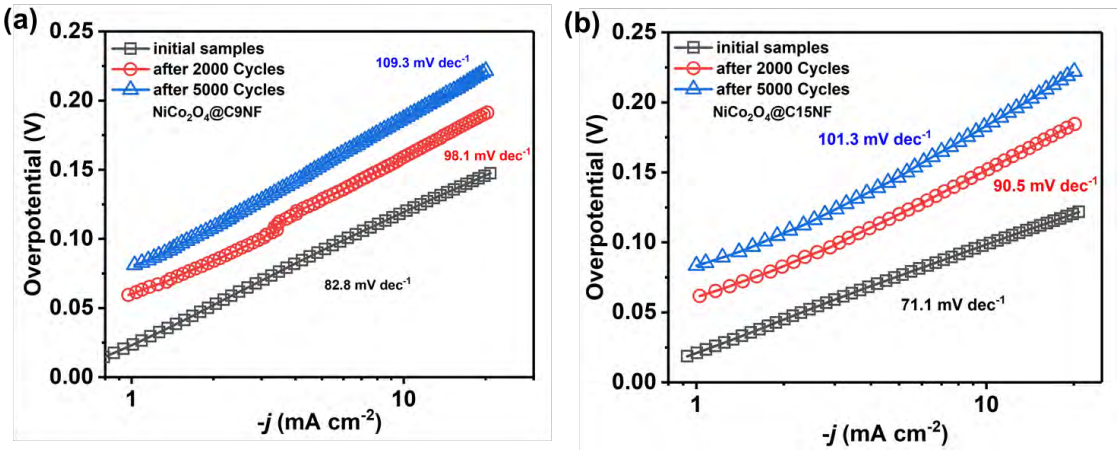

Fig. S9. Tafel plots.

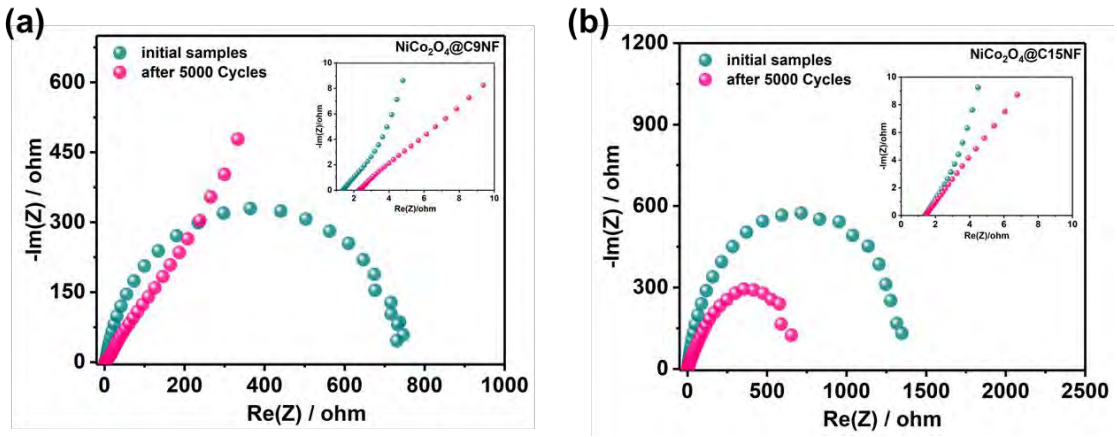

Fig. S10. Nyquist plots of $NiCo_2O_4$@C9NF and $NiCo_2O_4$@C15NF before and after CV.

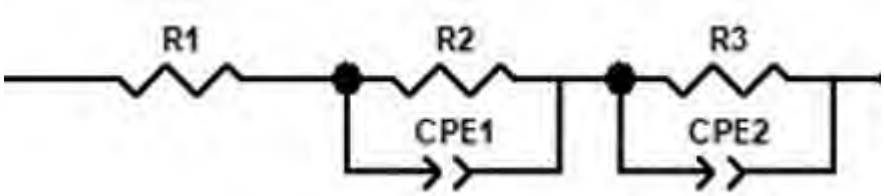

Fig S11 Fitting circuit in EIS map